

# Bidirectional Transformation Enables Hierarchical Nanolaminate Dual-Phase High-Entropy Alloys

Wenjun Lu, Christian H. Liebscher, Gerhard Dehm, Dierk Raabe, and Zhiming Li\*

Microstructural length-scale refinement is among the most efficient approaches to strengthen metallic materials. Conventional methods for refining microstructures generally involve grain size reduction via heavy cold working, compromising the material's ductility. Here, a fundamentally new approach that allows load-driven formation and permanent refinement of a hierarchical nanolaminate structure in a novel high-entropy alloy containing multiple principal elements is reported. This is achieved by triggering both, dynamic forward transformation from a face-centered-cubic  $\gamma$  matrix into a hexagonal-close-packed  $\epsilon$  nanolaminate structure and the dynamic reverse transformation from  $\epsilon$  into  $\gamma$ . This new mechanism is referred to as the "bidirectional transformation induced plasticity" (B-TRIP) effect, which is enabled through a near-zero yet positive stacking fault energy of  $\gamma$ . Modulation of directionality in the transformation is triggered by local dissipative heating and local micromechanical fields. The simple thermodynamic and kinetic foundations for the B-TRIP effect render this approach generally suited for designing metastable strong and ductile bulk materials with hierarchical nanolaminate substructures.

Metallic alloys are indispensable materials for multiple safety critical applications in manufacturing, transport, energy conversion, and medical devices. For bearing mechanical loads in often harsh environments they must be strong, tough, and formable. Achieving high strength and yet good ductility has long been a key issue in materials research.<sup>[1,2]</sup> One of the most efficient methods to strengthen metallic materials lies in microstructural refinement, exploiting various types of size-dependent strengthening mechanisms including the Hall–Petch effect, accumulation of geometrically necessary dislocations, and geometrical confinement of dislocation multiplication. The smaller the microstructural length scale, the higher is the required applied stress to propagate dislocations through the material.<sup>[3–5]</sup> However, many conventional microstructural refinement mechanisms usually compromise ductility of engineering alloys, e.g., Fe–C steel,<sup>[4]</sup> FeMnAlC steel,<sup>[6]</sup> Mg,<sup>[5]</sup> Al alloy,<sup>[7]</sup> and Ti–6Al–4V alloy,<sup>[8]</sup> as illustrated in **Figure 1**. Also, established methods such as severe plastic deformation usually require specific and size-limited processing equipment.<sup>[9,10]</sup> Further, metals with

conventional nanostructures, for instance with grain sizes below a critical value of  $\approx 50$  nm, can experience softening due to grain boundary sliding.<sup>[11,12]</sup>

Over the past years, a novel approach to microstructure design, known as hierarchical laminate structure, has shown to greatly improve strength and ductility of conventional materials simultaneously, such as Ti alloys and steels, through massive microstructure refinement.<sup>[13–16]</sup> Typically, such materials with hierarchical laminate structures consist of a parent phase serving as soft matrix to improve ductility and a hard product phase impeding dislocation motion to strengthen the microstructure. Unfortunately, such heterogeneous materials with high local mechanical disparity among their constituting phases are often prone to internal damage initiation, thus limiting ductility to 3.8–15% for Ti alloys,<sup>[13,14]</sup> 20–33% for


medium Mn steels,<sup>[17]</sup> and 23–33% for stainless steels.<sup>[16]</sup> Therefore, the mechanical properties of such hierarchical laminate materials need to be further improved to minimize the probability of internal damage and failure. Also, creating laminate structures in bulk materials often requires imposing complex processing methods, e.g., accumulative roll bonding.<sup>[18]</sup>

Interestingly, a recently developed dual-phase high-entropy alloy (HEA) also exhibits a simultaneous increase of strength and ductility after grain refinement<sup>[19–23]</sup> as highlighted in **Figure 1**. The excellent strength–ductility combination of the novel dual-phase HEA has been reported to be related to the transformation-induced plasticity (TRIP) effect, i.e., the displacive phase transformation from the face-centered cubic (FCC  $\gamma$ ) matrix into the hexagonal close-packed (HCP  $\epsilon$ ) phase upon deformation.<sup>[19,22]</sup>

Depending on the magnitude of the stacking fault energy, different compositional variants of recently developed HEAs have shown deformation modes with planar dislocation slip,<sup>[24,25]</sup> twinning induced plasticity (TWIP),<sup>[26]</sup> or TRIP effect.<sup>[22]</sup> Here, we observe another state which is thermodynamically characterized by a similar stability of two co-existing phases (FCC  $\gamma$  and HCP  $\epsilon$ ). This means that the stacking fault energy of the FCC matrix must assume a near-zero yet positive value so that forward ( $\gamma \rightarrow \epsilon$ ) and backward ( $\epsilon \rightarrow \gamma$ ) transformations can be both triggered in the same material and loading state.

We studied the deformation mechanisms in the dual-phase HEA (Fe<sub>50</sub>Mn<sub>30</sub>Co<sub>10</sub>Cr<sub>10</sub>, at%) in more detail via transmission electron microscopy (TEM) analysis and found that this novel TRIP-assisted HEA gradually develops a hierarchical

Dr. W. Lu, Dr. C. H. Liebscher, Prof. G. Dehm, Prof. D. Raabe, Dr. Z. Li  
Max-Planck-Institut für Eisenforschung  
Max-Planck-Straße 1, 40237 Düsseldorf, Germany  
E-mail: zhiming.li@mpie.de

 The ORCID identification number(s) for the author(s) of this article can be found under <https://doi.org/10.1002/adma.201804727>.

DOI: 10.1002/adma.201804727

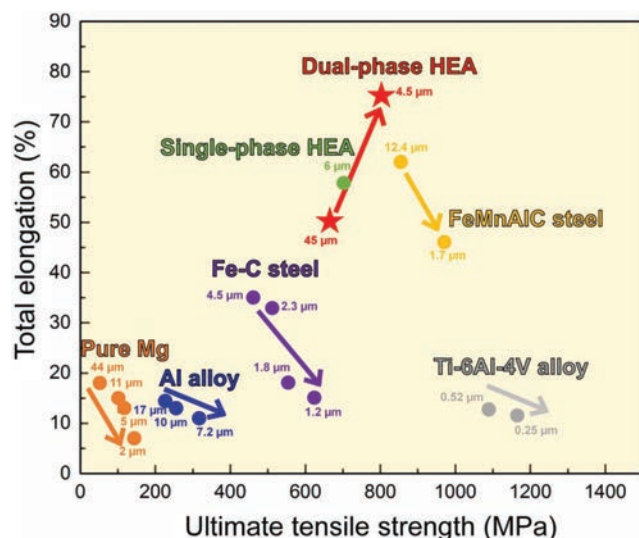


**Figure 1.** Strength and ductility profiles of different types of metallic materials. The TRIP-assisted dual-phase HEA shows the simultaneously increased strength and ductility by grain refinement, which contracts to the strength-ductility trade-off by grain refinement in conventional materials such as Fe-C steel, FeMnAlC steel, pure Mg, Al alloy, and Ti-6Al-4V alloy. All data stem from tensile tests conducted on bulk metallic materials at room temperature.

nanolaminate structure during loading, consisting of HCP  $\epsilon$  nanolaminates in the FCC  $\gamma$  blocks and FCC  $\gamma$  nanolaminates (with twin relation) in HCP  $\epsilon$  blocks. The profound difference

between metallic nanolaminate structures reported before and the one observed here is that it: i) consists of a dynamic forward and reverse TRIP effect among the two phases and thus ii) gradually keeps refining itself under mechanical loading. We refer to this new mechanism as Bidirectional Transformation Induced Plasticity (B-TRIP) effect. When reaching a self-organized laminate length scale on the order of 50 nm the alloy increases in strength with simultaneously improved ductility up to 77% elongation.

We also discuss the fundamental mechanisms responsible for the formation of the novel structure and related influencing factors such as stacking fault energy, local temperature and local stress-strain fields. We reveal two main factors enabling such hierarchical nanolaminate microstructures: i) It is required to thermodynamically tune the alloy into a state where the two phases  $\gamma$  and  $\epsilon$  have nearly the same stability, i.e., the associated athermal transformation barriers are so small that the microstructural stress states, thermal dissipation and dislocation patterns decide which phase is formed locally. ii) Kinetically the dynamic forward and backward transformations are realized by the motion of Shockley partial dislocations. These thermodynamic and kinetic insights provide guidance for creating such hierarchical nanolaminate substructures in a broader range of bulk materials for jointly improving strength and ductility.

We first reveal the structure of the dual-phase HEA processed by cold-rolling and recrystallization annealing followed by water-quenching, which contains HCP  $\epsilon$  phase with a volume fraction of  $\approx 34\%$  in the FCC  $\gamma$  matrix (see Figure S1, Supporting Information). **Figure 2a,b** displays the bright-field

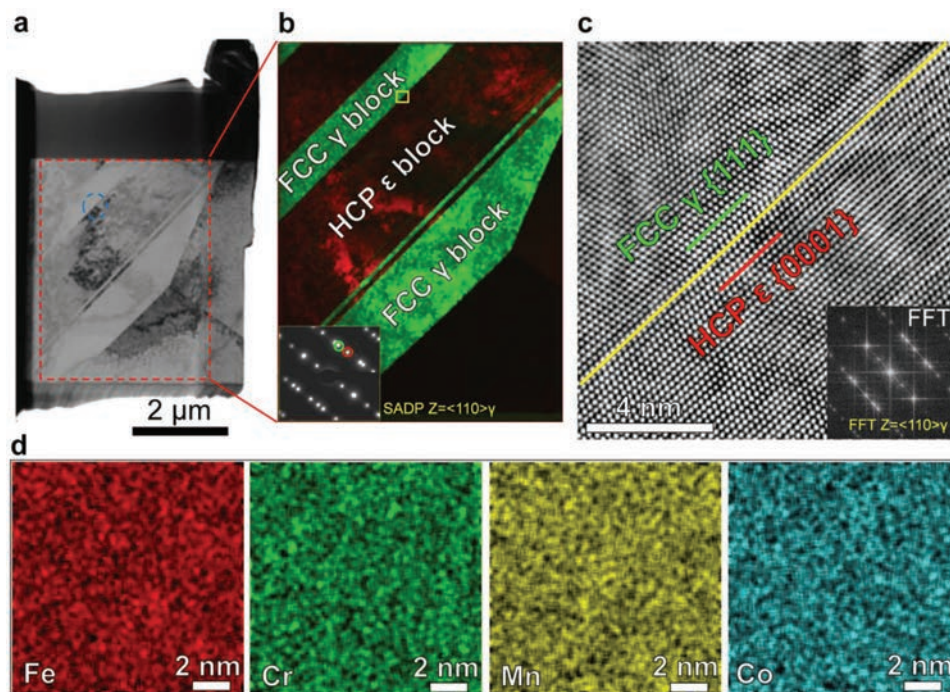


**Figure 2.** TEM/STEM analysis of the phase interface in the as-quenched HEA prior to deformation. a) Low-magnification bright-field TEM and b) the corresponding dark-field TEM images of the dual-phase structure containing FCC  $\gamma$  block in green and HCP  $\epsilon$  block in red. The inset in (b) shows a SADP taken from the circled region in (a) with objective aperture of  $\approx 400$  nm along the  $\langle 110 \rangle_{\gamma}$  zone axis. c) High-resolution HAADF-STEM image with the corresponding FFT pattern. The interface between FCC  $\gamma$  and HCP  $\epsilon$  blocks in (c) is highlighted by a yellow line. d) STEM-EDS maps with the identical sample region in (c) showing the distributions of the four principal elements, i.e., Fe, Cr, Mn, and Co. SADP, FFT, and EDS refer to the selected-area diffraction pattern, fast Fourier transform, and energy dispersive X-ray spectroscopy, respectively.



and dark-field TEM images of the quenched alloy sample, respectively, suggesting co-existence of HCP  $\epsilon$  (in red) and FCC  $\gamma$  blocks (in green). From the selected-area diffraction pattern (SADP) (inset in Figure 2b), the  $\{1\bar{1}01\}$  (red circle) and  $\{111\}$  (green circle) reflections are utilized to highlight  $\epsilon$  in red and  $\gamma$  in green, respectively. For the sample region marked by a yellow square in Figure 2b, the atomic-scale high-angle annular dark-field scanning mode in a transmission electron microscope (HAADF-STEM) image after bandpass filtering and the corresponding fast Fourier transform (FFT along  $\langle 110 \rangle_\gamma$  zone axis) are shown in Figure 2c. According to the high-resolution STEM image, the atomic columns of the HCP  $\epsilon$  and FCC  $\gamma$  blocks have a standard S-N orientation relationship, i.e.,  $\langle 11\bar{2}0 \rangle_\epsilon // \langle 110 \rangle_\gamma$  and  $\{0002\}_\epsilon // \{111\}_\gamma$ .<sup>[19,27]</sup> The uniform Z-contrast of the two phases suggests that there are no obvious atomic-scale compositional modulations. To further reveal the atomic-scale elemental distribution in the region of Figure 2c, STEM–energy-dispersive X-ray spectroscopy (EDS) analysis was performed and the results are displayed in Figure 2d. It is confirmed that the four principal elements, i.e., Fe, Mn, Co and Cr, are uniformly distributed over the two phases, suggesting that the phase transformation from the FCC  $\gamma$  matrix to the HCP  $\epsilon$

during water-quenching is displacive without elemental diffusion, even at the atomic scale.

Apart from the interface between the two phases ( $\gamma$  and  $\epsilon$ ) shown above, the internal structures of individual blocks ( $\epsilon$  and  $\gamma$ ) have also been characterized by TEM/STEM. Figure 3a presents a bright-field TEM image of another sample region containing HCP  $\epsilon$  and FCC  $\gamma$  blocks after water-quenching. A number of fine laminates inside both HCP  $\epsilon$  and FCC  $\gamma$  blocks are indicated by the green and red arrows in Figure 3a, respectively. To reveal the nature of the fine laminates, an SADP was taken and shown in Figure 3c. From the SADP, the fine laminates with average thickness of  $\approx 27$  nm in the HCP  $\epsilon$  blocks have FCC structure, and an S–N relationship between the  $\epsilon$  block and the  $\gamma$  laminate phases was confirmed. Similar to the HCP  $\epsilon$  block, the FCC block contains fine  $\epsilon$  laminates with an average thickness of  $\approx 56$  nm. To highlight the  $\gamma$  nanolaminates, Figure 3b illustrates the dark-field TEM image using one of the  $\{111\}$  reflections in the SADP shown in Figure 3c. The mean spacing between the  $\gamma$  nanolaminates is about  $88 \pm 5$  nm. The high-resolution HAADF-STEM image in Figure 3d shows that the  $\gamma$  nanolaminates can be as thin as several atomic layers, i.e., constituting stacking faults in the HCP  $\epsilon$  blocks.

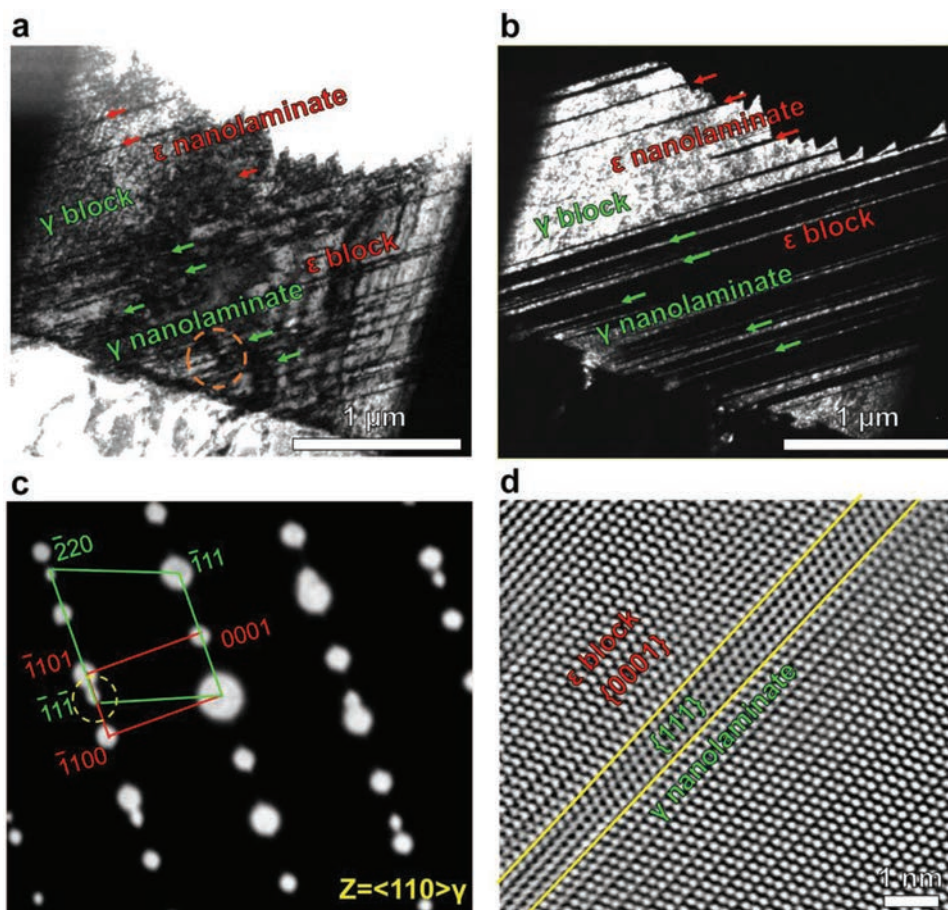


**Figure 3.** TEM/STEM analysis of the dual-phase HEA after water-quenching. a) The bright-field TEM and b) the dark-field TEM images of two blocks (FCC  $\gamma$  and HCP  $\epsilon$ ) containing nanoscale laminate features indicated by arrows. c) Experimental SADP combined with the simulated diffraction patterns along  $\langle 110 \rangle_\gamma$  zone axis. The simulated diffraction superlattice spots for  $\gamma$  and  $\epsilon$  are shown in green and red, respectively. d) High-resolution HAADF-STEM image of a  $\gamma$  nanolaminate within the HCP  $\epsilon$  block.

We next reveal the nanostructure of the FCC  $\gamma$  blocks in the dual-phase HEA after tensile deformation. **Figure 4a,b** shows the low- and high-magnification bright-field TEM images of an FCC  $\gamma$  block along the  $\langle 011 \rangle$  zone axis after tensile deformation with a local strain of 70%, respectively. **Figure 4c** gives the SADP taken from the sample region marked by an orange circle in **Figure 4a**. There are two variants of strain-induced  $\varepsilon$  nanolaminates ( $\varepsilon_1$  and  $\varepsilon_2$ ) with  $\{111\}$  habit planes in the deformed FCC  $\gamma$  block. The HAADF-STEM image in **Figure 4d** shows that even at the intersection of the  $\varepsilon$  laminate variants no body-centered cubic (BCC) martensitic phase is formed. This observation confirms that HCP  $\varepsilon$  is the only product phase of the transformation from the FCC  $\gamma$  blocks, and other martensite variants, e.g., BCC  $\alpha'$  observed in metastable steels,<sup>[28]</sup> do not exist in the current dual-phase HEA.

The bright-field TEM image in **Figure 5a** shows an overview of a typical HCP  $\varepsilon$  block taken from a sample region with a local strain of 70% after tensile deformation. The experimental SADP taken from the sample region marked by a white

circle and the corresponding simulated pattern are shown in **Figure 5b,c**, respectively. The diffractogram is composed of three sets of reflections stemming from the HCP  $\varepsilon$  block, the  $\gamma$  nanolaminates and the nanoscale  $\gamma$ -twins, respectively. The orientation relationship among these three structures is confirmed to be  $\langle 11\bar{2}0 \rangle_{\varepsilon} // \langle 110 \rangle_{\gamma} // \langle 110 \rangle_{\gamma\text{-twin}}$ ;  $\{0002\}_{\varepsilon} // \{111\}_{\gamma} // \{111\}_{\gamma\text{-twin}}$ . **Figure 5d-f** are dark-field TEM images of an identical sample region highlighting  $\{1\bar{1}00\}_{\varepsilon}$ ,  $\{200\}_{\gamma}$ , and  $\{200\}_{\gamma\text{-twin}}$ , respectively. The mean spacing of the  $\gamma$  nanolaminates (including twins) within this deformed HCP  $\varepsilon$  block was about  $46 \pm 3$  nm (**Figure 5e,f**), which is half of that in the quenched HCP  $\varepsilon$  block prior to deformation. This spacing difference is mainly due to the formation of nanoscale  $\gamma$ -twins during deformation.

We also performed an in situ deformation study using an in-house custom-designed Cu tensile holder (**Figure 6a**), imaging the microstructure in low angle annular dark-field scanning mode in a transmission electron microscope (LAADF-STEM). As shown in **Figure 6b**, a matrix grain (upper region) and a

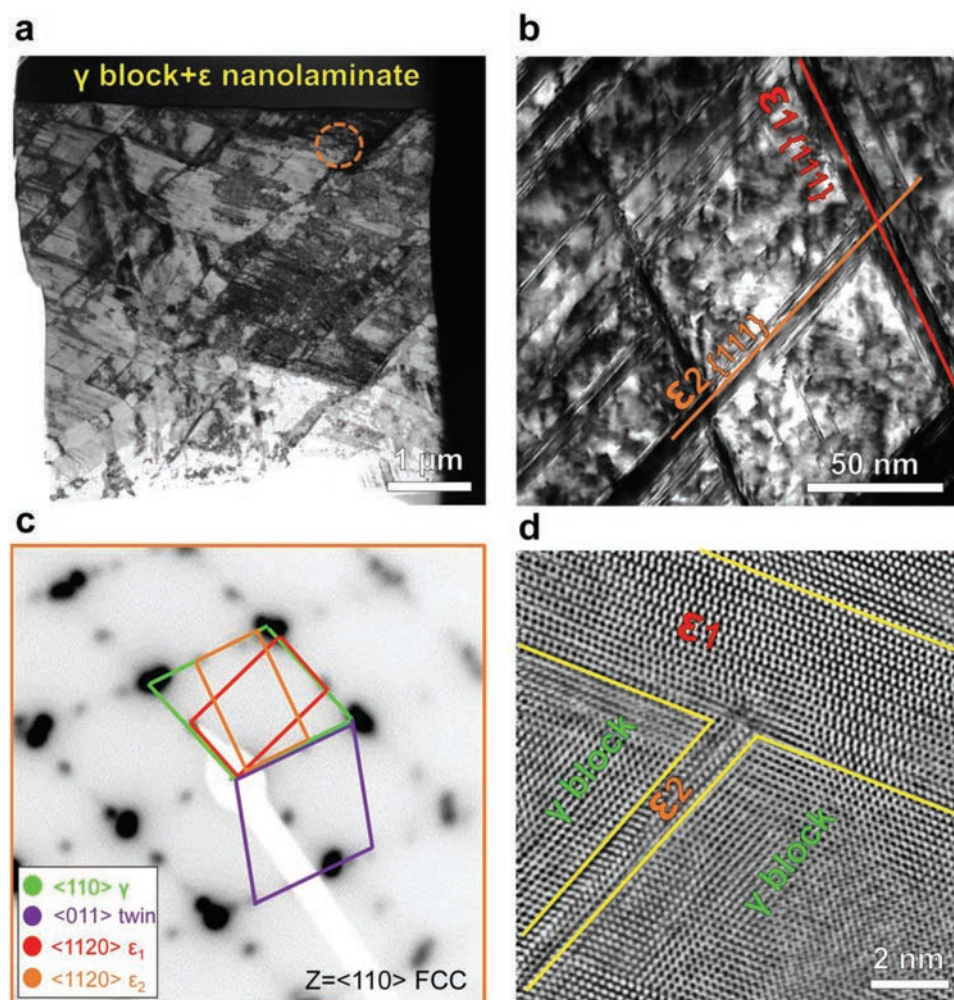


**Figure 4.** TEM/STEM analysis of an FCC  $\gamma$  block taken from a sample region with a local strain of 70% after tensile deformation. a) Low- and b) high-magnification bright-field TEM images of the deformed FCC  $\gamma$  block containing two variants of strain-induced  $\varepsilon$  nanolaminates ( $\varepsilon_1$  and  $\varepsilon_2$ ). c) SADP taken from the sample region marked by an orange circle in (a). d) High-resolution HAADF-STEM image of the intersection of two variants of strain-induced  $\varepsilon$  nanolaminates.



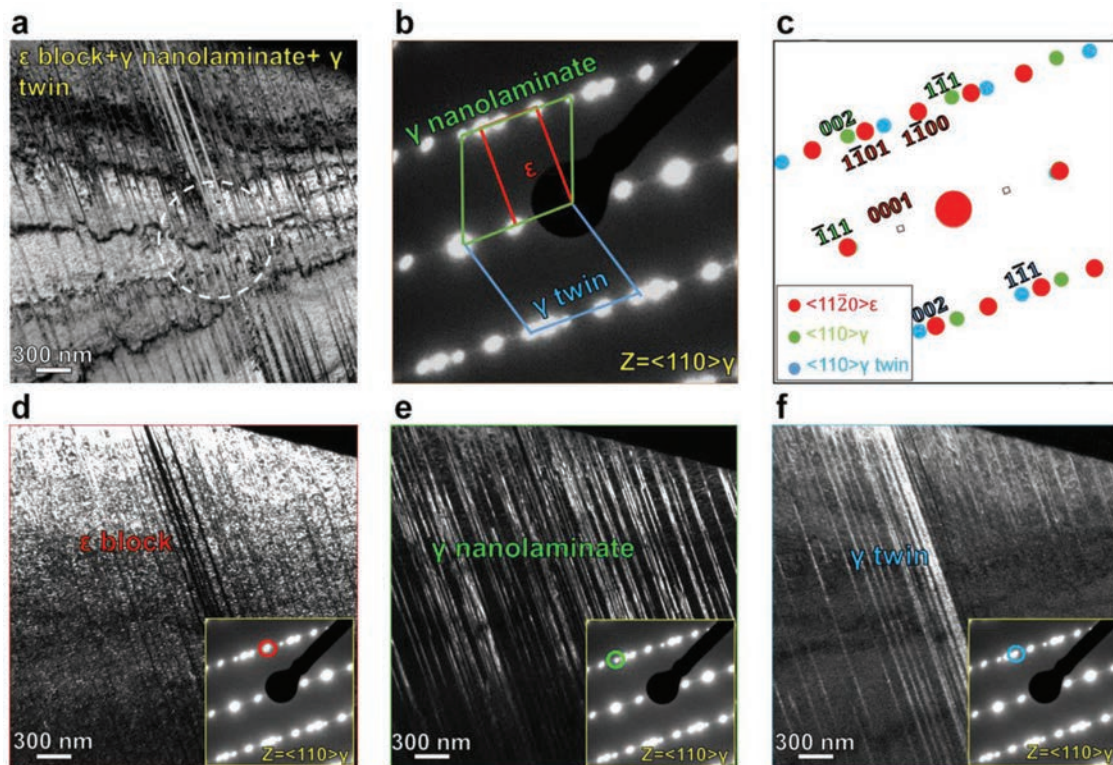


**Figure 5.** TEM analysis of an HCP  $\epsilon$  block with a local strain of 70%. a) A typical bright-field TEM image, b) SADP, and c) simulated diffraction patterns of the deformed HCP  $\epsilon$  block. d–f) Dark-field TEM images highlighted by the  $\epsilon$ ,  $\gamma$ , and  $\gamma$ -twin superlattice spots, respectively.

twin (lower region) with a  $\Sigma 3$  twin boundary marked by a red dashed line were captured. The inset in Figure 6b shows the corresponding SADP, indicating that the electron beam was close to the  $[110]$  and  $[011]$  zone axes for the matrix grain and the twin, respectively. There were two pre-existing variants of HCP  $\epsilon$  plates (V-1 and V-2) visible in the matrix grain. For simplicity we only focus on one variant of the HCP  $\epsilon$  plates (V-1), revealed by LAADF-STEM imaging in terms of strain contrast, Figure 6c. Based on the SADP analysis, the Schmid factor of the HCP  $\epsilon$  plates (V-1) along  $[\bar{2}11](\bar{1}\bar{1}\bar{1})$  has a positive value of about 0.1, which implies that the HCP  $\epsilon$  plates (V-1) are growing during straining via motion of their leading partial dislocations. Figure 6c shows the forward ( $\gamma \rightarrow \epsilon$ ) and reverse ( $\epsilon \rightarrow \gamma$ ) transformations during in situ deformation imaged under LAADF-STEM conditions. As shown in the initial stage of deformation (stage 1: 0 strain), no clear HCP  $\epsilon$  plates were visible. After tensile deformation to a low strain (stage 2), two HCP  $\epsilon$  plates indexed as HCP-1 and HCP-2 were detected and propagate along the  $[\bar{2}11](\bar{1}\bar{1}\bar{1})$  slip system towards the  $\Sigma 3$  twin boundary. Upon further straining (stage 3), a newly formed HCP  $\epsilon$  plate (HCP-3) was observed. This implies that a full dislocation was first nucleated in the matrix and then dissociated into two partial dislocations (i.e., a mobile leading and a sessile trailing) realizing the forward transformation. However, all HCP  $\epsilon$  plates (i.e., HCP-1, HCP-2, and HCP-3) generated by the forward transformation cannot penetrate through the  $\Sigma 3$  twin boundary and were stopped at the intersection zone between the  $[\bar{2}11](\bar{1}\bar{1}\bar{1})$  slip system and the  $\Sigma 3$  twin boundary plane at an intermediate tensile strain (stage 4). This indicates

that the  $\Sigma 3$  twin boundary can effectively block the transmission of the leading partial dislocations.<sup>[40,41]</sup> Upon further straining of the tensile specimen (stage 6), the HCP-1 plate disappeared followed by subsequent disappearance of the HCP-2 plate. Also, the HCP-3 plate was completely reversed and no retained stacking faults parallel to the  $[\bar{2}11](\bar{1}\bar{1}\bar{1})$  slip system were observed at a relatively high tensile strain (stage 8). Thus, this in situ STEM probing reveals the formation of HCP  $\epsilon$  nanolaminates and their reversion back to the FCC  $\gamma$  matrix, establishing a novel bi-directional TRIP effect.

Based on these observations we thus establish a novel deformation mechanism which is characterized by dynamic and adaptive forward ( $\gamma \rightarrow \epsilon$ ) and backward ( $\epsilon \rightarrow \gamma$ ) transformations under mechanical load. We refer to it as the “bidirectional transformation induced plasticity” (B-TRIP) effect. In the following we discuss the B-TRIP effect in more detail and preconditions for triggering it. The aim is to establish a novel, simple and efficient microstructure design concept for making strong and ductile bulk alloys with hierarchical nanolaminate substructures.

Schematic diagrams are shown in Figure S2 (Supporting Information) to provide an overview for the formation process of the hierarchical nanolaminate structure associated with the B-TRIP effect. In the quenched material, the dual-phase microstructure contains FCC  $\gamma$  and HCP  $\epsilon$  blocks (see Figure 2 and Figure S2b, Supporting Information). Since the alloy is characterized by a single FCC  $\gamma$  phase at 900°C (Figure S2a, Supporting Information), the HCP  $\epsilon$  block in the quenched alloy was produced via thermally-induced martensitic transformation<sup>[22]</sup> with a volume fraction of  $\approx 34\%$

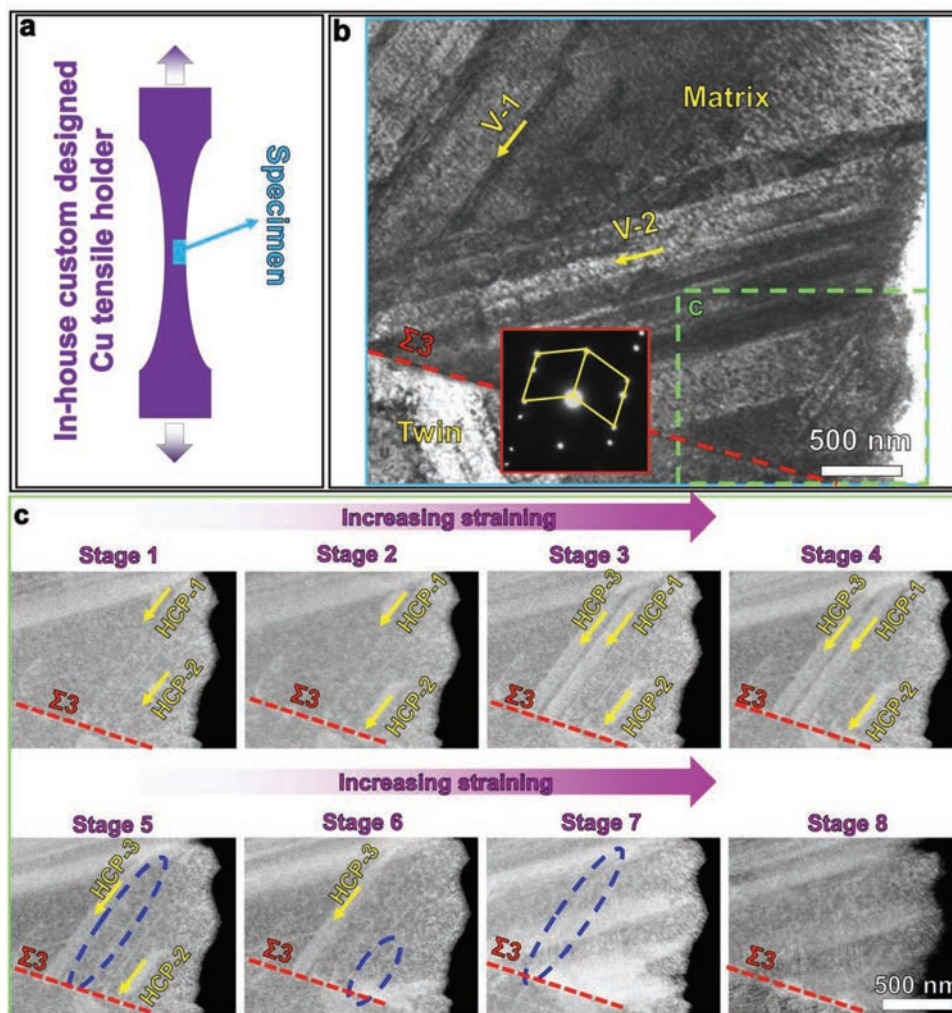


**Figure 6.** In situ deformation study conducted in the low angle annular dark-field scanning transmission electron microscope (LAADF-STEM). a) Schematic illustration of the in situ deformation set-up: an in-house custom-made Cu tensile holder (in purple) with a TEM specimen identifying the region of observation (in blue). b) TEM analysis prior to the in situ deformation: a bright-field TEM image showing a matrix grain (upper) and a twin (lower) with a  $\Sigma 3$  twin boundary marked by a red dashed line. The inset shows the corresponding selected area diffraction pattern (SADP), indicating that the electron beam was close to the  $[110]$  and  $[011]$  zone axes for the matrix grain and the twin, respectively. c) Series of in situ LAADF-STEM images of the forward ( $\gamma \rightarrow \epsilon$ ) and the reverse ( $\epsilon \rightarrow \gamma$ ) transformations in the dual-phase HEA during deformation with the increase of strain from low to high (stages 1–8). The red dashed lines, yellow arrows, and blue dashed circles denote the  $\Sigma 3$  twin boundary, the forward and the reverse transformations, respectively.

(Figure S1, Supporting Information). Both the FCC  $\gamma$  and HCP  $\epsilon$  blocks contain a number of  $\epsilon$  and  $\gamma$  nanolaminates along  $\{111\}$  FCC  $\gamma$  and  $\{0001\}$  HCP  $\epsilon$  habit planes, respectively (Figure 3 and Figure S2b, Supporting Information). After 70% local strain (see Figures 4 and 5, and Figure S2c, Supporting Information), the FCC  $\gamma$  blocks typically contain two different variants of  $\epsilon$  nanolaminates ( $\epsilon_1$  and  $\epsilon_2$ ). The  $\epsilon$  nanolaminates increase in number density while the mean spacing of the  $\gamma$  nanolaminates in the HCP  $\epsilon$  blocks is reduced from  $88 \pm 5$  to  $46 \pm 3$  nm at 70% local strain. The number density increase of the  $\epsilon$  nanolaminates in the FCC  $\gamma$  blocks can be interpreted by a strain-induced athermal transformation mechanism.<sup>[19,22,29]</sup> As schematically presented in Figure 7a, in an FCC  $\gamma$  block containing 12  $\{111\}$  atomic layers with ABCABC... sequence prior to mechanical loading, the strain-induced transformation

is initiated by the dissociation of a perfect  $\frac{1}{2}[110]$  dislocation into two Shockley partial dislocations, namely a leading  $\frac{1}{6}[211]$  partial and a trailing  $\frac{1}{6}[12\bar{1}]$  partial.<sup>[29,30]</sup> The transformation proceeds on every second  $\{111\}$  atomic plane, hence creating a bilayer HCP  $\epsilon$  phase (i.e., intrinsic stacking fault) with BC sequence.<sup>[31]</sup> Accordingly, after three steps, a strain-induced  $\epsilon$  nanolaminate with six atomic layers thickness (BCBC...) is generated by this transformation (Figure 7a). Based on this mechanism,  $\epsilon$  nanolaminates with even numbers of atomic layers can be produced. Accordingly, Figure 7b gives three examples of strain-induced  $\epsilon$  nanolaminates (6, 20, and 36 atomic layers with BCBC... sequence) inside the deformed FCC  $\gamma$  block (ABCABC... sequence) characterized by high-resolution HAADF-STEM.



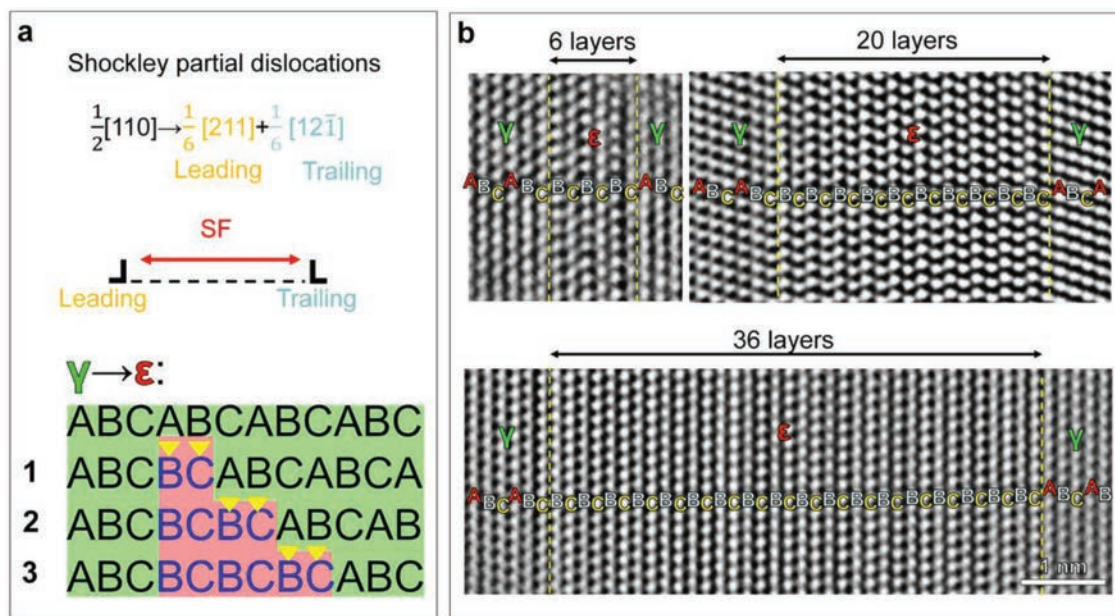


**Figure 7.** Illustration of the forward  $\gamma \rightarrow \epsilon$  transformation mechanism. a) Schematics showing the separation of two Shockley partial dislocations (leading and trailing) from a perfect dislocation results in a stacking fault (SF). The numbers “1”, “2,” and “3” represent the steps after the gliding of partials over along the  $\{111\}$  planes. The green and red regions are FCC  $\gamma$  (ABCABC... sequence) and HCP  $\epsilon$  (BCBC... sequence) phases, respectively. b) High-resolution HAADF-STEM images of the strain-induced  $\epsilon$  nanolaminates with 6, 20, and 36 atomic layers in FCC  $\gamma$  block after deformation.

Interestingly, this  $\gamma \rightarrow \epsilon$  transformation mechanism does not necessarily explain the occurrence of  $\gamma$  nanolaminates inside the HCP  $\epsilon$  blocks after deformation. This may rather be due to a reverse transformation ( $\epsilon \rightarrow \gamma$ )<sup>[27,32–35]</sup> inside the HCP  $\epsilon$  block. In order to discuss this hypothesis, three factors, viz., the stacking fault energy,<sup>[30]</sup> local temperature,<sup>[32]</sup> and local stress-strain fields,<sup>[27]</sup> have to be considered.

We first discuss the stacking fault energy, i.e., the energy associated with the interruption of the regular ABCABC... stacking sequence in the FCC  $\gamma$  structure of the dual-phase HEA.<sup>[21]</sup> In general, an intrinsic stacking fault energy (SFE) for FCC  $\gamma$  structure is expressed as  $SFE = 2\rho(\Delta G^{\gamma-\epsilon} + E^{\text{str}}) + 2\sigma^{\gamma-\epsilon}$ , where  $\Delta G^{\gamma-\epsilon}$  is the Gibbs molar free energy difference mentioned above ( $-420 \text{ J mol}^{-1}$ ),  $E^{\text{str}}$  is the strain energy of the transformation ( $22.2 \text{ J mol}^{-1}$ ).  $\sigma^{\gamma-\epsilon}$  is the coherent  $\gamma$ - $\epsilon$  interfacial energy ( $15 \text{ mJ m}^{-2}$ )<sup>[21]</sup> and  $\rho$  is the planar packing density (moles/area) of a close-packed plane  $\{111\}$ , i.e.,  $\rho = \frac{4}{\sqrt{3}} \frac{1}{a^2 N} = 2.96 \times 10^{-5} \text{ mol m}^{-2}$

based on the lattice constant of the FCC  $\gamma$  phase (3.6 Å) and Avogadro's number  $N$  ( $6.02 \times 10^{23}$ ). The stacking fault energy of the dual-phase HEA is thus calculated to be  $6.5 \text{ mJ m}^{-2}$ . Such a small yet positive stacking fault energy has a high possibility to initiate reverse transformation ( $\epsilon \rightarrow \gamma$ ) as all associated influence factors such as the local dissipative heating, other lattice defects acting as pinning points for dissociated partials, local stress fields and possible stacking fault partitioning effects may alter the local delicate partial separation and phase equilibrium, influencing it locally either towards the FCC or the HCP phase.<sup>[30]</sup> This is due to the fact that such a low value of the stacking fault energy renders the stability among the two phases (FCC  $\gamma$  and HCP  $\epsilon$ ) nearly identical, so that local stress or temperature can affect this balance. A higher stacking fault energy (e.g.,  $>15 \text{ mJ m}^{-2}$ )

usually leads to planar dislocation patterns and deformation twinning in FCC structures, while a smaller stacking fault energy ( $<15 \text{ mJ m}^{-2}$ ) can lead to the dissociation of the dislocations into two partials and stacking faults between them.<sup>[36]</sup> However, the separation can be reversed via the motion of the trailing partial dislocations even when the stacking fault energy is very low as long as the stacking fault energy has a positive value,<sup>[30]</sup> as demonstrated here for the dual-phase HEA with a stacking fault energy of  $\approx 6.5 \text{ mJ m}^{-2}$ . This provides the possibility for the joint activation of the forward ( $\gamma \rightarrow \epsilon$ ) and backward ( $\epsilon \rightarrow \gamma$ ) transformations (B-TRIP effect) and the formation of the hierarchical nanolaminate structure as well as its permanent refinement in the same material and loading state. A negative stacking fault energy leads presumably rather to a transformation in only one direction without any reversibility, as evidenced in Co-Cr-Mo alloys.<sup>[29]</sup> Our observation further suggests that, to achieve the B-TRIP effect, the stacking fault energy of the FCC matrix must assume a near-zero yet positive value. It is important to note that the stacking fault energy dependent B-TRIP effect in the current dual-phase HEA only involves transformations between FCC  $\gamma$  and HCP  $\epsilon$ , which is fundamentally different from the conventional TRIP effect in steels containing body centered or tetragonal  $\alpha'$  as the final transformation product phase. This observation suggests that tuning of similar phase stability of the FCC  $\gamma$  and the HCP  $\epsilon$  to suppress the formation of BCC  $\alpha'$  phase seems to be important for triggering the B-TRIP effect (instead of a unidirectional TRIP effect) and the associated hierarchical nanolaminate structure. In other words the deformation-driven transformation between FCC  $\gamma$  and HCP  $\epsilon$  is mutually reversible in the current alloy while the transformation sequence FCC  $\gamma \rightarrow$  HCP  $\epsilon \rightarrow$  BCC  $\alpha'$ , known from many steels, is not reversible.

Second we discuss the effect of dissipative heating on the reverse transformation from  $\epsilon$  to  $\gamma$ . As mentioned above, the Gibbs free energy difference between the HCP  $\epsilon$  and FCC  $\gamma$  phases has a negative value, suggesting that  $\epsilon$  is more stable than  $\gamma$  at room temperature. No reverse transformation ( $\epsilon \rightarrow \gamma$ ) will take place unless other driving forces act, e.g., local mechanical stresses and/or local temperature increase during straining.<sup>[32]</sup> The dissipative heating during straining

can be estimated by  $\Delta T = \frac{\beta}{\rho C_p} W(\epsilon)$ , where  $C_p$  is the specific heat capacity of the dual-phase HEA at room temperature ( $\approx 0.444 \text{ J g}^{-1} \text{ K}^{-1}$ ) according to that of an alloy with similar composition,<sup>[37]</sup>  $\rho$  is the mass density ( $7.732 \text{ g cm}^{-3}$ ),  $\beta$  is the conversion efficiency between mechanical work and heat ( $\approx 0.9$ ),  $W(\epsilon)$  is the deformation work calculated by the local stress and strain. With a local strain of 70% the estimated local heating amounts to a value of 141 K. When the SFE is so low ( $\approx 6.5 \text{ mJ m}^{-2}$ ) as supposed in the current dual-phase HEA, the variation in dissipative heating may influence—together with local stresses and microstructure pinning points—the direction in which the local phase fractions develop, i.e., either promoting the FCC  $\gamma$  or the HCP  $\epsilon$  phases.

We thus finally discuss the effect of local stress–strain fields on the reverse transformation ( $\epsilon \rightarrow \gamma$ ). Theoretically, a reverse transformation from the HCP  $\epsilon$  to the FCC  $\gamma$  can be achieved through the motion of Shockley partials on every second  $\{0001\}$  basal plane with Burgers vectors  $\frac{a}{3} \langle 1\bar{1}00 \rangle$ .<sup>[27]</sup> They have three equivalent glide directions, which can generate stacking faults (i.e., nanoscale FCC structure) in the HCP matrix with negligible volume expansion.<sup>[27,33,34]</sup> Upon strain loading, the sliding of Shockley partials in the HCP  $\epsilon$  block of the dual-phase HEA is achieved by two possible ways (**Figure 8**). Figure 8a shows a possible reverse transformation (process 1) caused by the motion of a leading partial dislocation with higher Schmid factor compared to the trailing partial dislocation.<sup>[30]</sup> After the motion of three leading partial dislocations, six atomic layers of the FCC  $\gamma$  phase with ABCABC... stacking sequence can be created. When the Schmid factor of the trailing partial dislocation is higher than that of leading partial dislocation, another reverse transformation (process 2) from a BCBC... HCP  $\epsilon$  phase to a CBACBA... FCC  $\gamma$  phase can be initiated as schematically shown in Figure 8b. These newly formed FCC  $\gamma$  phase regions with CBACBA... stacking sequence have a twin-relation with the original FCC  $\gamma$  phases with ABCABC... sequence. Three FCC  $\gamma$ -twins with respectively 8, 10 and 16 atomic layers have been characterized by high-resolution HAADF-STEM imaging and displayed in Figure 8c. Thus, the reverse transformation mechanisms ( $\epsilon \rightarrow \gamma$ ) can be activated by the motion of partial dislocations including both leading and trailing ones, depending on their respective Schmid factors.

Through such a B-TRIP effect, the strength and ductility of the dual-phase HEA can be simultaneously improved.<sup>[19]</sup> This is mainly ascribed to a hierarchical laminate structure consisting of a parent phase of FCC  $\gamma$  serving as softer matrix to improve ductility and a harder HCP  $\epsilon$  product phase impeding dislocation motion, thus strengthening the microstructure. During deformation, the hierarchical laminate structure is continuously self-refining, providing high work hardening capacity. Another important point that seems to contribute to the high ductility of

the dual-phase HEA lies in the deformation-driven reversibility of the transformation. This effect is a very important micromechanical mechanism in that context since local stress peaks that can otherwise lead to damage initiation and hence to premature failure can in the current material relax by reversing the transformation. This means that transformation reversion acts here as a self-accommodation mechanism which can better redistribute lattice defect arrangements in damage-critical regions where the local stresses get very high. Hence, the B-TRIP effect is probably a good structure relaxation vehicle of a material to adapt to locally critical microstructure arrangements that would otherwise—in nonadaptive microstructures—lead to failure initiation.

In summary, we revealed and explained a new dynamic deformation and transformation mechanism which we refer to as B-TRIP effect. Different from conventional transformation and twinning induced plasticity effects, the B-TRIP effect is characterized by permanent microstructure refinement due to multiple forward ( $\gamma \rightarrow \epsilon$ ) and reverse ( $\epsilon \rightarrow \gamma$ ) deformation-driven transformations events. This leads to the formation of a hierarchical nanolaminate structure and its permanent refinement, providing extensive work hardening capacity and hence strengthening material without sacrificing ductility, shown here for a dual-phase nonequiatomic high-entropy alloy. The B-TRIP effect is mainly controlled by the stacking fault energy, local temperature and local stress–strain fields. The results provide a new paradigm for designing bulk metallic alloys with high density of hierarchical nanolaminates with excellent combination of strength and ductility without any need of imposing complex processing.

## Experimental Details

A 1 kg ingot of the quaternary dual-phase HEA with a nominal composition of Fe-30Mn-10Co-10Cr (at%) was first cast in a vacuum induction furnace using pure metals (>99.5 wt% pure). Alloy plates with thickness of 10 mm were cut from the original cast block and then hot rolled at 900 °C to a thickness of 5 mm. The rolled band was subsequently homogenized for 2 h at 1200 °C in Ar atmosphere followed by water-quenching. The chemical composition of the homogenized alloy sample was determined by wet-chemical analysis as Fe-28.5Mn-11.1Co-9.77Cr (wt%). The contents of impurity elements Cu, Ni, Mo, Sb, Sn, C, N, O, P, and S in wt% were determined to be 0.333, 0.0114, <0.002, <0.001, <0.01, 0.0064, 0.0077, 0.025, <0.001 and 0.0063, respectively. To obtain alloy samples with appropriate grain sizes and phase fractions, the homogenized alloy was cold-rolled to a thickness of 2 mm (60% reduction ratio) and then annealed at 900 °C in an Ar protected furnace for 60 min followed by water-quenching. The alloy samples were then metallographically ground using silicon carbide abrasive paper from the grit size P600 to P4000, followed by polishing using 3 and 1  $\mu\text{m}$  diamond suspensions and 50 nm silicon oxide polishing suspension. The alloy samples were finally cleaned by ethanol to remove the extra nano-silica particles.

The microstructure of the alloy samples was characterized using multiple techniques. XRD measurements were performed using an X-ray diffractometer (ISO-DEBYEFLEX 3003)



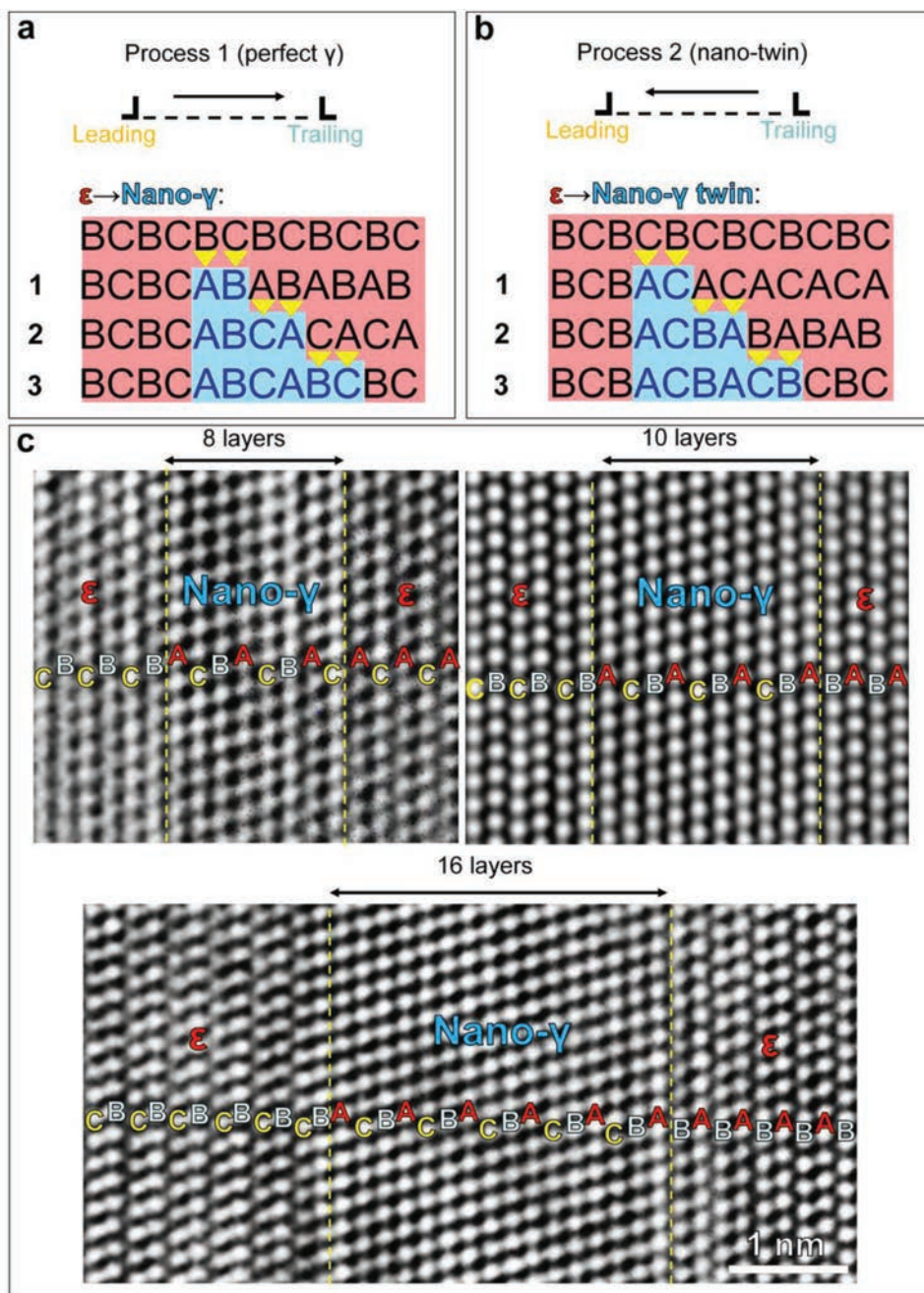


**Figure 8.** Reverse transformations ( $\epsilon \rightarrow \gamma$ ) caused by the motion of partial dislocations (leading or trailing) during deformation. a) Schematic showing the formation of six atomic layer FCC  $\gamma$  with ABCABC... stacking sequence and b) schematic showing the formation of six atomic layer  $\gamma$ -twin with CBACBA... stacking sequence. c) The high-resolution HAADF-STEM images of nanoscale  $\gamma$ -twins with 8, 10, and 16 atomic layers.

with Co  $K_{\alpha 1}$  ( $\lambda = 1.788965 \text{ \AA}$ ) radiation. Electron backscatter diffraction measurements were carried out by means of a JEOL-6500 FEG-SEM using 50 nm step size and 15 kV acceleration voltage. A Phillips CM20 TEM operated at 200 kV accelerating voltage was used to analyze TEM foils by bright/dark-field imaging and SADP. The TEM foils were prepared by a site specific focused ion beam (FIB) lift-out procedure<sup>[38]</sup> with a final cleaning voltage about 5 kV in a dual-beam FIB instrument (FEI Helios Nanolab 600i). STEM imaging and STEM-EDS were conducted in an aberration-corrected STEM/

TEM (FEI Titan Themis) at an acceleration voltage of 300 kV. For high-resolution imaging a probe semi-convergence angle of 17 mrad and the inner and outer semi-collection angles of the annular detector from 73 to 350 mrad were chosen. The room temperature in situ deformation in the low angle annular dark-field (LAADF)-STEM was conducted using a Gatan model 654 single-tilt straining holder in an image-corrected FEI Titan Themis 80–300 operated at 300 kV. The upper loading direction was  $[\bar{5}5\bar{9}]$ . The detailed procedures of the in situ TEM deformation are described by Lee et al.<sup>[39]</sup> For the LAADF-STEM

imaging, a probe semi-convergence angle of 17 mrad and inner and outer semi-collection angles from 14 to 63 mrad were used. In order to observe the microstructure of the alloy sample after macro-tensile deformation, rectangular dog-bone-shaped samples were cut by electrical discharge machining with a thickness of 1 mm, a gage length of 10 mm and a width of 2.5 mm. Kammrath & Weiss tensile stage was utilized to perform the digital image correction assisted uniaxial tensile tests at ambient temperature and at a strain rate of  $1 \times 10^{-3} \text{ s}^{-1}$ .

## Supporting Information

Supporting Information is available from the Wiley Online Library or from the author.

## Acknowledgements

This work was financially supported by the European Research Council under the EU's 7th Framework Programme (FP7/2007-2013)/ERC Grant agreement 290998.

## Conflict of Interest

The authors declare no conflict of interest.

## Keywords

dual phase, hierarchical nanolaminate structures, high-entropy alloys, phase transformation, scanning transmission electron microscopy

Received: July 23, 2018  
Revised: August 21, 2018  
Published online:

- [1] K. Lu, *Science* **2014**, *345*, 1455.  
[2] J. Hu, Y. N. Shi, X. Sauvage, K. Lu, *Science* **2017**, *355*, 1292.  
[3] L. Lu, Y. Shen, X. Chen, L. Qian, K. Lu, *Science* **2004**, *304*, 422.  
[4] S. Takaki, *Mater. Sci. Forum* **2010**, *654–656*, 11.  
[5] M. Diez, H-E. Kim, V. Serebryany, S. Dobatkin, Y. Estrin, *Mater. Sci. Eng., A* **2014**, *612*, 287.  
[6] A. Etienne, V. Massardier-Jourdan, S. Cazottes, X. Garat, M. Soler, I. Zuazo, X. Kleber, *Metall. Mater. Trans. A* **2013**, *45*, 324.  
[7] A. S. Golezani, R. V. Barenji, A. Heidarzadeh, H. Pouraliakbar, *Int. J. Adv. Manuf. Technol.* **2015**, *81*, 1155.  
[8] W. Xu, E. W. Lui, A. Pateras, M. Qian, M. Brandt, *Acta Mater.* **2017**, *125*, 390.  
[9] Y. Estrin, A. Vinogradov, *Acta Mater.* **2013**, *61*, 782.  
[10] A. Azushima, R. Kopp, A. Korhonen, D. Y. Yang, F. Micari, G. D. Lahoti, P. Groche, J. Yanagimoto, N. Tsuji, A. Rosochowski, A. Yanagida, *CIRP Ann.* **2008**, *57*, 716.  
[11] K. Lu, W. D. Wei, J. T. Wang, *Scr. Mater.* **1990**, *24*, 2319.  
[12] H. Conrad, J. Narayan, *Scr. Mater.* **2000**, *42*, 1025.  
[13] M. Li, D. Guo, T. Ma, Y. Shi, G. Zhang, X. Zhang, *Mater. Sci. Eng., A* **2014**, *606*, 396.  
[14] Y. Shi, L. Wang, C. Wu, *J. Mater. Eng. Perform.* **2015**, *24*, 5054.  
[15] M. Koyama, Z. Zhang, M. M. Wang, D. Ponge, D. Raabe, K. Tsuzaki, H. Noguchi, C. C. Tasan, *Science* **2017**, *355*, 1055.  
[16] S. C. Cao, J. Liu, L. Zhu, L. Li, M. Dao, J. Lu, R. O. Ritchie, *Sci. Rep.* **2018**, *8*, 5088.  
[17] M. M. Wang, C. C. Tasan, D. Ponge, A. C. Dippel, D. Raabe, *Acta Mater.* **2015**, *85*, 216.  
[18] H. Chang, M. Y. Zheng, W. M. Gan, K. Wu, E. Maawad, H. G. Brokmeier, *Scr. Mater.* **2009**, *61*, 717.  
[19] Z. Li, K. G. Pradeep, Y. Deng, D. Raabe, C. C. Tasan, *Nature* **2016**, *534*, 227.  
[20] Z. Li, F. Körmann, B. Grabowski, J. Neugebauer, D. Raabe, *Acta Mater.* **2017**, *136*, 262.  
[21] Z. Li, D. Raabe, *JOM* **2017**, *69*, 2099.  
[22] Z. Li, C. C. Tasan, K. G. Pradeep, D. Raabe, *Acta Mater.* **2017**, *131*, 323.  
[23] M. M. Wang, Z. Li, D. Raabe, *Acta Mater.* **2018**, *147*, 236.  
[24] F. Otto, A. Dlouhý, C. Somsen, H. Bei, G. Eggeler, E. P. George, *Acta Mater.* **2013**, *61*, 5743.  
[25] Y. Zhang, T. T. Zuo, Z. Tang, M. C. Gao, K. A. Dahmen, P. K. Liaw, Z. P. Lu, *Prog. Mater. Sci.* **2014**, *61*, 1.  
[26] Y. Deng, C. C. Tasan, K. G. Pradeep, H. Springer, A. Kostka, D. Raabe, *Acta Mater.* **2015**, *94*, 124.  
[27] H. Zhao, M. Song, S. Ni, S. Shao, J. Wang, X. Liao, *Acta Mater.* **2017**, *131*, 271.  
[28] X-S. Yang, S. Sun, T-Y. Zhang, *Acta Mater.* **2015**, *95*, 264.  
[29] Y. Koizumi, S. Suzuki, K. Yamanaka, B-S. Lee, K. Sato, Y. Li, S. Kurosu, H. Matsumoto, A. Chiba, *Acta Mater.* **2013**, *61*, 1648.  
[30] T. Mitsunobu, Y. Koizumi, B-S. Lee, A. Chiba, *Scr. Mater.* **2014**, *74*, 52.  
[31] O. G. B. Olson, C. M. Cohen, *Metall. Mater. Trans. A* **1976**, *7A*, 1897.  
[32] J. Y. Li, W. Li, M. J. Jin, X. J. Jin, *Mater. Re. Lett.* **2014**, *3*, 107.  
[33] Q. Yu, J. Kacher, C. Gammer, R. Traylor, A. Samanta, Z. Yang, A. M. Minor, *Scr. Mater.* **2017**, *140*, 9.  
[34] H. Zhao, X. Hu, M. Song, S. Ni, *Scr. Mater.* **2017**, *132*, 63.  
[35] H. T. Wang, N. R. Tao, *Scr. Mater.* **2018**, *145*, 109.  
[36] P. Chowdhury, D. Canadinc, H. Sehitoglu, *Mater. Sci. Eng., R* **2017**, *122*, 1.  
[37] Y. Brif, M. Thomas, I. Todd, *Scr. Mater.* **2015**, *99*, 93.  
[38] C. H. Liebscher, V. R. Radmilović, U. Dahmen, N. Q. Vo, D. C. Dunand, M. Asta, G. Ghosh, *Acta Mater.* **2015**, *92*, 220.  
[39] S. Lee, J. Im, Y. Yoo, E. Bitzek, D. Kiener, G. Richter, B. Kim, S. H. Oh, *Nat. Commun.* **2014**, *5*, 3033.  
[40] K. Lu, L. Lu, S. Suresh, *Science* **2009**, *324*, 349.  
[41] L. Lu, X. Chen, K. Lu, *Science* **2009**, *323*, 607.